A reassessment of the stress and natural fracture orientations from analysis of image logs in the Chinese Continental Scientific Drilling Program borehole at Donghai county, Jiangsu province, China

Miao Luo[a, b*], Paul W.J. Glover[b], Heping Pan[a]

[a]Hubei Subsurface Multi-scale Imaging Key Lab, Institute of Geophysics and Geomatics, China University of Geosciences, Wuhan 430074, China

[b]School of Earth and Environment, University of Leeds, Leeds LS2 9JT, UK

Abstract

The Chinese Continental Scientific Drilling (CCSD) project has drilled a 5100 m deep research borehole in the Sulu ultra-high pressure (UHP) metamorphic belt, eastern China. The UHP metamorphic belt is thought to be a product of continent-continent collision and has consequently experienced very intensive structural deformation. Based on a more complete well log data set of CCSD borehole, we can have a more detailed and reliable study on the structure features of borehole wall and other rock physical properties than a previous study published in 2009. Abundant data related to borehole breakouts (BOs), drilling induced tensile fractures (DITFs) and natural fractures were collected from the image logs. The BO and DITF data indicate that the average direction of the maximum horizontal principal stress (S_H) of the CCSD borehole site is about 79.2° which is consistent with the convergent direction (E-W) of the Pacific Sea Plate with respect to the Eurasian Plate. Analysis of DITFs indicated that in the case of the CCSD borehole, axial drilling induced tensile fractures (ADITFs) occur occasionally in the upper section (0-2300 m) of the borehole with low dipping angle (0-10°), while transverse drilling induced tensile fractures (TDITFs) occur significantly in the lower section (3800-5000 m) with high dipping angle (10-30°). The natural fracture distribution at depth in the metamorphic rocks of the CCSD borehole indicates that (1) the failure strength of rocks and borehole depth are two factors that affects natural fracture frequency, (2) most of the dip azimuth of natural fractures is consistent with the dip azimuth of foliations observed in the core, (3) the development of most of the natural fractures probably was dominated by the development of foliations, and both the natural

fractures and foliations developed in response to the subduction and exhumation of the Sulu terrene.

Keywords: continental deep drilling; image logs; stress orientation; borehole breakout; drilling induced tensile fracture; natural fracture distribution

1. Introduction

Knowledge of the in-situ stress state of the formation and Earth crust is very important for the study of borehole stability (Zoback et al., 2003; Zhang et al., 2009; Tingay et al., 2009; Zhang, 2013), hydraulic fracture stimulation (Haimson and Fairhurst, 1967; Maxwell et al., 2009; Davies et al., 2012; Schmitt and Haimson, 2016; Rajabi et al., 2017), well path design (Goodman and Connolly, 2007), water flooding (Nelson, 2005), and earthquake fault system evolution (Stein, 1999; Sandiford, 2003; Sibson et al, 2011; Nie et al, 2013).

When studying the stress field of the Earth crust, researchers often assume an Andersonian (1951) state of stress with that the direction of one of the principal stresses is vertical, so the three orthogonal principal stresses are: (i) a vertical stress (S_V), (ii) a maximum (S_H) and (iii) a minimum horizontal principal stress (S_h) (Schmitt et al., 2012). The direction of S_H is a key parameter in the study of the present formation stress and regional stress field. Under the impact of contemporary stress field, borehole breakouts (BOs) occur when the hoop stress around the borehole wall exceeds the compressive strength of the borehole wall rocks (Bell and Gough, 1979; Zoback et al, 1985) (Fig. 1a). Meanwhile, drilling induced tensile fractures (DITFs) occur when the hoop stress around the borehole wall exceeds that required to cause tensile failure of the borehole wall (Fig. 1a). A great number of investigations have shown that the orientation of BOs indicates the direction of the S_h and that of DITFs indicates the direction of the S_H for a vertical or near-vertical well within an Andersonian stress state (Fig. 1b) (Bell and Gough, 1979; Gough and Bell, 1982; Blumling et al., 1983; Plumb and Hiekman, 1985; Hickman et al., 1985; Zoback et al, 1985; Haimson and Herrick, 1986; Vernik and Zoback, 1992; Aadnøy and Bell, 1998; Nelson, et al., 2005). Subsequently, borehole image logs have been widely used to identify BOs and DITFs that are related to the in-situ S_H and ascertain the S_H direction (Wu, et al., 2007; Tingay et al., 2008; Rajabi, et al., 2010; Lin et al. 2010; Nie, et al., 2013).

Cui et al. (2009) has studied the present tectonic stress state of the Chinese Continental Scientific Drilling (CCSD) wellbore site by using borehole cross-section data collected from acoustic image logs. Their study indicates that the direction of the S_H of the CCSD wellbore site is 49.5±3.5°. However, the world stress map indicates that the direction of the S_H at the CCSD wellbore site is close to 80°. Thus, it is necessary to carry out more work at this wellbore site.

In this study, we use both resistivity and ultrasonic image logs to obtain the BO and DITF data and fracture distribution of the CCSD borehole, and then calculate the direction of the S_H in the CCSD borehole in its present stress state. The fracture distribution in the borehole is probably related to the in-situ lithology and its structure, which are, in turn, related to the subduction and exhumation process of the Sulu ultra-high pressure metamorphic (UHPM) belt and can be used to study the evolution of the Sulu UHPM belt.

2. Geological setting

From 2001 to 2005 the Chinese government carried out a Chinese Continental Scientific Drilling (CCSD) project to drill a vertical borehole in the southern part of the Sulu ultra-high pressure metamorphic (UHPM) belt (N34°25′, E118°40′), about 30 km east of the Tan-Lu fault and 17 km southwest of Donghai County, as shown in Fig. 2.

The Dabie-Sulu UHPM belt is the largest recognized UHPM belts in the world. It has become an ideal geological area for studying ultra-high pressure (UHP) metamorphism and geodynamic mechanisms of continental subduction and exhumation since the discovery of coesite-bearing eclogites (Okey et al., 1989; Wang et al., 1989) and diamond-bearing eclogites (Xu et al., 1992). The Dabie-Sulu UHPM belt was formed by the Triassic collision of the Sino-Korean and Yangtze craton with the peak metamorphic age of 220-245 Ma (Ames et al., 1996; Hacker et al., 1998; Rowley et al., 1997). The UHPM rocks of the Dabie-Sulu metamorphic belt have been subducted to at least 100 km and have experienced UHP metamorphism before being rapidly exhumed from mantle depths and back to the surface.

The Sulu UHPM belt is commonly considered to be the eastern extension of the Qinling-Dabie orogen. It is separated from the Sino-Korean craton to the NW by the Yantai-Qingdao-Wulian Fault (YQWF), and the Yangtze craton to the SE by the Jiashan-Xiangshui Fault (JXF). The Sulu terrane consists of two metamorphic units: the northern UHPM belt and the southern high-pressure metamorphic belt (Zhang et al., 1995) (Fig. 2).

The principal lithologies of the CCSD borehole include orthogneiss, paragneiss, eclogite, and amphibolite together with minor amounts of ultramafic rock (Fig. 3). A detailed description of the lithology and petrology is given by Liu et al. (2004).

The crystalline rocks of the CCSD borehole are hard and non-permeable, and consequently the borehole shape varies little due to interactions between the drilling bit, the drilling mud and the various lithologies through which the hole passes. The stability of the borehole wall depends more on the formation stress and the development of fracture zones.

From a global point of view, the study area is located at the east part of the Eurasian Plate (Fig. 2). Taking the Eurasian Plate as a reference, the Pacific Plate moves towards the WNW and the Philippine Sea Plate moves towards the NW at present (Zhou and Ding, 1995; Kimura et al., 2009). The east part of the Eurasian Plate is undergoing a strong compressive stress field. Therefore, the CCSD borehole provides a very good opportunity to study the stress state of the east part of the Eurasian Plate.

3. Methodology

3.1. Image log data acquisition

The CCSD project carried out rigorous drilling and logging programme, and obtained a large amount of high-quality core and well log data which provides us with an excellent opportunity to study the fracture distribution in the borehole and the in-situ stress state of the borehole site. The well log data of the CCSD borehole were acquired by the ECLIPS-5700 image logging system of Baker Hughes and the MAX-500 image logging system of Schlumberger. Fig. 3 shows some conventional logs, such as gamma ray (GR), acoustic velocity (V_P), density (DEN), deep resistivity (RD) and caliper (CAL). The images of the CCSD borehole wall were obtained by resistivity and ultrasonic image logging tools. All the logging tools were calibrated regularly to ensure its accuracy. Both the resistivity and ultrasonic image logging tools contain orientation measurement device which can record the azimuth of the tool in real time and output the unrolled pseudo-image of the borehole wall oriented to the geographic north (0°) (Fig. 4).

The resistivity image tools are pad tools that measure the formation micro resistivity directly through an array of resistivity buttons mounted on pads that are pressed against the borehole wall (Ekstrom et al, 1987). For the Schlumberger Fullbore Formation MicroImager (FMI): vertical resolution: 5 mm; vertical sampling: 0.25 mm; depth of investigation: 76 mm (Schlumberger, Ltd., 1994).

The ultrasonic imaging tools send sound pulses out to the formation by a transducer and measure both the amplitude and the travel time of the returning signals reflected by the borehole wall. The ultrasonic transducer can rotate continually and make 360° scanning. For the Schlumberger Ultra-Sonic Borehole Imager: azimuthal resolution: 2°; vertical resolution from 0.5 mm to 25.4 mm depending on pulse frequency (500 to 250 kHz); depth of investigation: 0 (Gaillot, et al., 2007).

The ultrasonic imaging tools can perform well in both oil-based and water-based mud, but the resistivity imaging tools only in water-based (conductive) mud. In addition, ultrasonic image logs could be easily affected by borehole roughness or washouts.

3.2. Borehole breakouts and drilling induced tensile fractures

With the resistivity and ultrasonic (amplitude) image logs, we can identify borehole wall breakouts (BOs), drilling induced tensile fractures (DITFs) and natural fractures (NFs) in the CCSD borehole (Fig. 4).

Previous studies proved that drilling induced tensile fractures (DITFs) fall into two types: axial (vertical) drilling induced tensile fractures (ADITFs) and transverse drilling induced tensile fractures (TDITFs) (Aadnøy and Bell, 1998; Brudy and Zoback, 1999). ADITFs usually appear in vertical wells (the borehole axis is parallel to a principal stress), while

TDITFs usually occur in dipping wells (the borehole trajectory does not lie along a principal stress direction) (Zoback, 2007, Schmitt et al., 2012).

In Fig. 4a, the two vertical dark bands on the image with a difference in their direction of 180 degree correspond to the borehole wall breakouts (BOs). In Fig. 4b, the two near-vertical fractures apart 180 degree are axial drilling induced tensile fractures (ADITFs). In Fig. 4c, the two groups of short fractures apart 180 degree with en-echelon structure are transverse drilling induced tensile fractures (TDITFs).

For a vertical well, the direction of S_H is perpendicular to that of the BO and parallel to that of the DITF (Zoback, 2007, Schmitt et al., 2012; Rajabi et al., 2017). Therefore, we can determine the direction of S_H of the drilling site of the CCSD borehole by studying the azimuthal direction of BOs and DITFs in the borehole.

3.3. Nature fractures and foliations

Natural fractures and foliations usually appear as sinusoidal stripes on the resistivity and ultrasonic image logs (Rider, 1996; Glover and Bormann, 2007; Serra, 2008).

In Fig. 5, both the resistivity and ultrasonic image logs present a dark quasi-sinusoidal stripe which indicates there is a natural fracture at 232 m of the CCSD borehole. The dip azimuth can be inferred from the lowest point of the quasi-sinusoidal stripe. In our case, the dip azimuth is measured clockwise looking down the borehole from the geographic north. Consequently, the dip azimuth of the fracture in Fig. 5 is approximately 200°.

Foliation in geology refers to repetitive layering in metamorphic rocks. It is caused by shearing forces (pressures pushing different sections of the rock in different directions), or differential pressure (higher pressure from one direction than in others) (Stephen, 2009).

Foliations can induce the development of natural fractures, so there are lots of natural fractures parallel to the foliations (Massiot et al., 2018).

In Fig. 6, serial parallel dark and bright stripes on the FMI image indicate foliations. The foliations display more crowded and continuous parallel structures than the natural fractures. Furthermore, the foliations usually do not have very high resistivity and ultrasonic amplitude contrast and display very weak logging anomaly and can only be observed sometimes on the image logs. Due to the limitation of the logging tools' resolution, we cannot observe foliations in most of the image logs of the CCSD borehole. Therefore, the studies of foliations usually depend on the core. However, the natural fractures usually display lower resistivity and sonic reflection amplitude than the surrounding rocks, so they have obvious features on both resistivity and ultrasonic image logs and are relatively easy to be identified.

With the assistance of high-quality image logs and conventional well logs, the azimuth and depth of cores can be restored (Fig. 5 and Fig. 6). Then, the true attitude information of planar and linear structures on the cores can be obtained, which makes the core more valuable. Conversely, the core images can be used to check the resolution and quality of the image logs.

4. Results and discussion

4.1. Orientation of the present S_H

Analysis of the Formation Micro-resistivity Image (FMI) and Ultra-Sonic Image (USI) logs from the CCSD borehole has allowed us to recognize 206 occurrences of breakout (BO) and 26 occurrences of drilling induced tensile fracture (DITF). Fig. 7a and b show the orientation distribution of BO and DITF with the depth in the CCSD borehole, while Fig. 7c shows the orientation of S_H derived from the orientation of BO and DITF, respectively.

The azimuthal direction of most BOs (θ_{BO}) ranges from 150 to 180° with an arithmetic mean of θ_{BO}= 168.6° and a standard deviation of $\sigma_{\theta BO}$=17.9°. The azimuthal direction of most DITFs (θ_{DITF}) ranges from 80° to 90° with an arithmetic mean of θ_{DITF}=83.3° and a standard deviation of $\sigma_{\theta DITF}$=12.3°. Consequently, the arithmetic mean of the azimuthal direction of S_H θ_{HB} and θ_{HD} for values derived from BOs and DITFs, respectively, are 78.6±17.9° and 83.3±12.3°. It is clear that the azimuthal directions of S_H derived from BOs and DITFs overlap significantly. In fact an unpaired t-test taking into account arithmetic means, standard deviations and the number of samples in each set shows there to be no statistical difference between them. The calculated P-value was 0.09 (or 9%), which is greater than 0.05 (5%), the common threshold for considering 2 populations to be different. Accordingly, we can justify taking the arithmetic mean of data for both BOs and DITFs to give a final value of θ_{SH} = 79.2±17.4°. This degree of error classifies the overall azimuthal direction of horizontal principle stress results presented in this work as having 'Quality B', according to world stress map guidelines (Heidbach et al., 2016) while the individual results from BOs and DITFs, have 'Quality A' and 'Quality B', respectively.

Our result (θ_{SH}= 79.2±17.4°) agrees with most of the data from the adjacent areas, as shown in Fig. 8, and is close to the E-W convergence direction between the Eurasian Plate and the Pacific Plate (Fig. 1). Feng et al. (2017) studied the recent tectonic stress field at the shallow earth's crust near the Tan-Lu fault zone. Their work indicted that the orientation of the principal compressive stress of the present tectonic stress field near the CCSD borehole area is N70°E which is close to our results.

The value we have calculated, however, is considerably different from the value of

θ_{SH}=49.5±3.5° reported by Cui et al. (2009). Application of an unpaired t-test to the combined 232 BO and DITF data from this work and the 143 well bore breakouts from Cui et al. (2009) provides P<0.0001, indicating that there is less than a 0.1% chance of the two studies being in agreement. This apparent variance clearly needs to be understood.

We have checked the causes of the difference between our results and that of Cui et al. (2009). The study of Cui et al. (2009) used 143 borehole cross-sections collected from the raw data of ultrasonic image logs which had not been processed, and only analysed well bore breakouts. Furthermore, selected depths were chosen at random for the recognition, or not, of borehole breakouts. By contrast, we have processed and analysed all of our image logs to provide (i) cleaner images which will reduce or eliminate some errors caused by reading unprocessed image log data, and (ii) a continuous coverage for the recognition of borehole breakouts and DITFs over the whole depth range of the data. In our case, we identified BOs using both resistivity image logs and ultrasonic image logs, leading to a more robust and reliable identification of well bore breakouts. Not only we have recognised 206 occurrences of well bore breakouts, but we also obtained 26 occurrences of DITF, which have been analysed independently, and as we have noted above agree very well with the well for breakout data. Consequently, this paper implements information from 232 orientable events in the borehole compared to 143 for Cui et al. (2009), i.e., 89 more. Consequently, we attribute the difference in our results compared to previous studies to our use of a greater number of orientation data, obtained from multiple events (BO and DITF) using two different types of fully processed image logs.

Axial drilling induced tensile fractures (ADITFs) and transverse drilling induced tensile fractures (TDITFs) are commonly encountered in image logs. Aadnøy and Bell (1998) gave a detailed classification of the borehole wall fractures and explained their origin. Fig. 7b shows that in the case of the CCSD borehole, ADITFs occur occasionally in the upper section (0-2300 m) of the borehole, while TDITFs occur significantly in the lower section (3800-5000 m). Fig. 7e shows that the deviation of the upper section (0-2300 m) of the borehole is restricted to the range 0-10°, while that of the lower section (3800-5000 m) is greater, in the range 10-30°.

It has already been recognised that ADITFs usually develop in vertical and slightly dipping wells while TDITFs tend to occur in more deviated wells (Aadnøy and Bell, 1998; Brudy and Zoback, 1999; Zoback, 2007, Schmitt et al., 2012). While we are disadvantaged by a lack of data in the 3000-3600 m range, combining the results from Fig. 3b and e, suggests that we can define a critical deviation angle below which ADITFs are more likely to occur and above which TDITFs are more likely to occur. For the CCSD borehole, the critical deviation angle seems to be approximately 10°.

4.2. Magnitude of formation stress

Within an Andersonian stress state, the direction of one of the principal stresses is vertical because the surface is a free boundary and the gravitational acceleration is directed downwards. The magnitude of the vertical stress (S_V) can be calculate by the equation

$$S_V(h)=\int_0^h \rho(h)g\mathrm{d}h \tag{1}$$

where h denotes the borehole depth, g denotes the gravitational acceleration, ρ denotes the density of rocks.

Fig. 7f displays the magnitudes of S_V, S_H and S_h versus depth. The magnitude of S_V was calculated by density log. According to the stress state around the borehole and Navier–Coulomb criterion, Zoback et al. (1985) developed two equations to estimate the magnitudes of S_H and S_h based on the rock strength parameters and borehole breakout geometry, Cui et al. (2009) employed the two equations and calculated the magnitudes of S_H

and S_h by core mechanical tests and borehole cross section data which derived from the ultrasonic image logs. The magnitude relationship (S_H>S_V>S_h) of the three principal stresses indicates that the regional stress field around the CCSD borehole is in a strike slip regime. This is consistent with the previous study (Wan, et al., 1996; Zhu, et al., 2004, Deng, et al., 2013).

4.3. Distribution of fracture dip azimuth and frequency

Numerous natural fractures are observed from the image logs of the CCSD borehole. Fig. 9a shows the distribution of the dip azimuth of natural fractures encountered by the borehole. Fig. 9b indicates that the fracture frequency of the 0-3000 m interval is greater than that of the 3600-5000 m interval, so the depth can be a potential factor that affects fracture frequency. In addition, the depth intervals (e.g. 1180-1220 m, 2200-2300 m) with very high fracture frequency occur in paragneiss and orthogneiss. We infer that this is attributed to the low-density and low-uniaxial failure strength of gneiss. The average density of gneiss and eclogite are 2.6 and 3.5 g/cm^3, respectively (Sun et al., 2012). The density log also showed that the density of the 0-3000 m interval is greater than that of the 3000-5000 m interval (Fig. 3). The average uniaxial failure strengths of gneiss and eclogite are 110.03 and 143.47 MPa, respectively (Cui et al., 2009).

To study the variation of fracture dip azimuth, we have split the well into 8 depth intervals (Table 1). These intervals are the same as used by Xu et al. (2009) when they divided the CCSD borehole into 6 big ‘petro-structure’ units according to the lithology and the petrophysical properties of the core before reporting the dip azimuth of foliation of each unit.

We have analyzed the dip azimuth of natural fractures for each of these 8 petrofacies units, and shown it as rose diagrams in Fig. 10, noting that image data was missing in the depth range 3000 to 3600 m, where no analysis could be carried out. Most of the depth ranges exhibit a similar dip azimuth of natural fractures as can be seen in Fig. 10. Table 1 indicate that the dip azimuth of natural fractures is similar with that of the foliations except unit D. Fig. 10g indicates that the dip azimuth of natural fractures is about 200° in the depth range 3623-5000 m, but Fig. 11h indicates that the dip azimuth of foliations is about 110° in the depth range 3225-5158 m. The lithology of 3623-5000 m interval is mainly composed of orthogneiss. Overall, we can conclude that the foliation direction could affect the development of natural fractures greatly in our study borehole and most of the natural fractures probably develop from the foliations (earlier ductile deformation) of the UHPM rocks.

The study of Xu et al. (2009) showed that the forming of foliations with a dip azimuth of 110±10° is the result of the subduction and exhumation of the Sulu terrene. Therefore, we can infer that most of the natural fractures with a dip azimuth of 110±20° in the CCSD borehole are developed in the subduction and exhumation process of the Sulu terrene. In addition, the evolution of the nearby NNE-striking Tan-Lu fault could affect the development of the natural fractures in the CCSD borehole too and probably generate some high dip angle fractures with NNE-striking.

5. Conclusion

Abundant high-quality resistivity and ultrasonic image logs were obtained from the CCSD borehole. These data have been analysed in order to recognise breakouts (BOs) and drilling induced tensile fractures (DITFs) as well as natural fractures. Furthermore, the azimuthal orientation (θ_{SH}) of the maximum horizontal principal stress (S_H) has been computed using the BO and DITF information.

There was no discernible difference in the azimuthal orientation (θ_{SH}) of the S_H when computed by using borehole BO data or by using DITF data. It has confirmed that there was no statistically significantly difference by subjecting the 2 datasets to a t-test (at a level of significance of 0.05). The mean value for the azimuth direction of the S_H is θ_{SH} =79.2±17.4°. This value is consistent with existing data on the World Stress Map and it is concluded that the present orientation of S_H in the study area is dominated by the E-W collision between the Pacific Plate and the Eurasian Plate.

Analysis of DITFs has indicated that there probably exists a critical well deviation angle, below which ADITFs mainly occur and above which TDITFs occur. In the case of the CCSD borehole, ADITFs occur in the upper section (0-2300 m) of the borehole whose dipping angle is less than 10°, while TDITFs occur in the lower section (3800-5000 m) of the borehole whose dipping angle is larger than 10°.

The magnitude relationship ($S_H > S_V > S_h$) of the three principal stresses indicates that the regional stress field around the CCSD borehole is in a strike slip regime.

The depth intervals (e.g. 1180-1220 m, 2200-2300 m) with very high fracture frequency occur in paragneiss and orthogneiss whose density and uniaxial failure strength are lower than the other rocks in the CCSD borehole, so the failure strength should be a very important factor that affects fracture frequency. Furthermore, the fracture frequency of the 0-3000 m interval is greater than that of the 3600-5000 m interval, so the depth could be a potential factor that affects fracture frequency.

The dip azimuth of natural fractures in the well ranges mainly between 90 to 180° in the 0-5000 m interval and is consistent with the dip azimuth of foliation observed in the core by other researchers (Xu et al., 2009). We infer that the natural fractures and the foliation both developed in response to the subduction and exhumation of the Sulu terrene and the development of foliations affects the development of natural fractures greatly.

Acknowledgements

This study was supported by the National Natural Science Foundation of China (No. 41574121, 41104080) and the China Scholarship Council. Thanks to the CCSD project center for providing well log and core data. We acknowledge the editors and reviewers for their constructive suggestions and comments.

References

Aadnøy, B.S., Bell, J.S., 1998. Classification of drilling-induced fractures and their relationship to in-situ stress directions. The Log Analyst, 39, 27–42.

Ames, L., Zhou, G., Xiong, B., 1996. Geochronology and Isotopic Character of Ultrahigh-Pressure Metamorphism with Implications for Collision of the Sino-Korean and Yangtze Cratons, Central China. Tectonics, 15, 472–489.

Anderson, E.M., 1951. The Dynamics of Faulting and Dyke Formation with Applications to Britain, 2nd Ed, Oliver and Boyd, Edinburgh, pp.10-22.

Bell, J.S., Gough, D.I., 1979. Northeast-southwest compressive stress in Alberta—evidence from oil wells. Earth and Planetary Sciences Letters, 45, 475-482.

Blumling, P., Fuchs, K., Schneider, T., 1983.Orientation of the stress field from breakouts in a crystalline well in a seismic active area. Physics of the Earth and Planetary Interiors, 33, 250-254.

Brudy, M., Zoback, M.D. 1999. Drilling-induced tensile wall fractures: implications for determination of in-situ stress orientation and magnitude. International Journal of Rock Mechanics and Mining Sciences, 36, 191-215.

Cui, J., Wang, L., Li, P., Tang, Z., Sun, D., 2009. Wellbore breakouts of the main borehole of Chinese Continental Scientific Drilling (CCSD) and determination of the present tectonic stress state. Tectonophysics, 475, 220-225

Davies, R.J., Mathias, S.A., Moss, J., Hustoft, S., Newport, L., 2012. Hydraulic fractures: how far can they go? Marine and Petroleum Geology, 37 (1), 1-6.

Deng, Y., Fan, W., Zhang, Z., Badal, J., 2013. Geophysical evidence on segmentation of the Tancheng-Lujiang fault and its implications on the lithosphere evolution in East China. Journal of Asian Earth Sciences, 78, 263-276

Ekstrom, M. P., Dahan, C., Chen, M. Y., Lloyd, P., and Rossi, D. J., 1987. Formation imaging with microelectrical scanning arrays. Log Analyst, 28, 294-306.

Feng, C., Zhang, P., Qi, B., Meng, J., Tan, C., Hu, G., 2017. Recent Tectonic Stress Field at the Shallow Earth's Crust near the Tan-Lu Fault Zone. Geoscience, 31(1): 46-68 (in Chinese with English abstract).

Gaillot, P., Brewer, T., Pezard, P., Yeh, E.C., 2007. Technical Developments Borehole Imaging Tools - Principles and Applications. Scientific Drilling 5, 1-4.

Glover, P., Bormann, P., 2007. The characterization of trough and planar cross-bedding from borehole image logs. Journal of Applied Geophysics, 62, 178–191.

Goodman, H. E., Connolly, P., 2007. Reconciling subsurface uncertainty with the appropriate well design using the mechanical Earth model (MEM) approach. The Leading Edge, 26, 585–588.

Gough, D.I., Bell, J.S., 1982. Stress orientations from oil-well fractures with examples from Colorado, east Texas, and northern Canada. Canadian Journal of Earth Sciences, 19, 1358-1370.

Hacker, B. R., Ratschbacher, L., Webb, L., Ireland, T., Walker,D., Dong, S., 1998. U/Pb zircon ages constrain the architecture of the ultrahigh-pressure Qinling–Dabie Orogen, China. Earth and Planetary Science Letters, 161, 215–230.

Haimson, B.C. and Fairhurst, C., 1967, Initiation and extension of hydraulic fractures in rocks. Society of Petroleum Engineering Journal 7, 310-318.

Haimson, B. C. and C. G. Herrick. 1986. Borehole breakouts — a new tool for estimating In-Situ stress? Proc., Int. Symp. on Rock Stress and Rock Measurements, Stockholm, A.A. Balkema, 271-278.

Heidbach, O., Rajabi, M., Reiter, K., Ziegler, M., WSM-Team, 2016. World Stress Map Database Release 2016. GFZ Data Services. http://doi.org/10.5880/WSM.2016.001.

Hickman, S.H., Healy, J.H., Zoback, M.D., 1985. In situ stress, natural fracture distribution, and borehole elongation in the Auburn Geothermal Well, Auburn, New York. Journal of Geophysics Research, 90, 5497–5512.

Kimura, H., Kasahara, K., Takeda, T, 2009. Subduction process of the Philippine Sea Plate off the Kanto district, central Japan, as revealed by plate structure and repeating earthquakes. Tectonophysics, 472, 18-27

Liu, F. L., Xu, Z. Q., Xue, H. M., 2004. Tracing the Protolith, UHP Metamorphism, and Exhumation Ages of Orthogneiss from the SW Sulu Terrane (Eastern China): SHRIMP U-Pb Dating of Mineral Inclusion-Bearing Zircons. Lithos, 78, 411–429.

Liu, F. L., Xu, Z. Q., Liou, J.G., Dong, H.L., Xue, H. M., 2007. Ultrahigh-Pressure Mineral Assemblages in Zircons from the Surface to 5158 m Depth in Cores of the Main Drill Hole, Chinese Continental Scientific Drilling Project, Southwestern Sulu Belt, China. International Geology Review, 49, 454-478.

Massiot, C., Celerier, B., Doan, M.-L., Little, T.A., McNamara, D.D., Townend, J., Schmitt, D.R., Williams, J., Toy, V.G., Sutherland, R., Janku-Capova, L., Upton, P., and Pezard, P., 2018. The Alpine Fault hangingwall viewed from within: structural analysis of acoustic image logs in the DFDP-2B borehole, New Zealand. Geochemistry, Geophysics, Geosystems, doi 2017GC007368.

Maxwell, S.C., Zimmer, U., Gusek, R.W., Quirk, D.J., 2009. Evidence of a Horizontal Hydraulic Fracture From Stress Rotations Across a Thrust Fault. SPE Production & Operations, 24, 312-319.

Nie, X., Zou, C., Pan, L., Huang, Z., Liu, D., 2013. Fracture analysis and determination of in-situ stress direction from resistivity and acoustic image logs and core data in the Wenchuan Earthquake Fault Scientific Drilling Borehole-2 (50-1370 m). Tectonophysics, 593, 161-171.

Nelson, E.J., Meyer, J.J., Hillis, R.R., Mildren, S.D., 2005. Transverse drilling-induced tensile fractures in the West Tuna area, Gippsland Basin, Australia: implications for the in situ stress regime. International Journal of Rock Mechanics & Mining Sciences, 42, 361-371.

Okey, A. I., Xu, S. T., Sengor, A. M. C., 1989. Coesite from the Dabie Shan Eclogites, Central China. European Journal of Mineralogy, 1, 595–598.

Plumb, R.A., Hiekman, S.H., 1985. Stress-induced borehole elongation: a comparison between the four-arm dipmeter and the borehole televiewer in the Auburn geothermal well. Journal of Geophysical Research, 90, 5513-5521.

Rajabi, M., Sherkati, S., Bohloli, B., Tingay, M., 2010. Subsurface fracture analysis and determination of in-situ stress direction using FMI logs: an example from the Santonian carbonates (Ilam Formation) in the Abadan Plain, Iran. Tectonophysics, 492, 192-200.

Rajabi, M., Tingay, M., Heidbach, O., Hillis, R., Reynolds, S., 2017. The present-day stress field of Australia. Earth Science Review 168, 165-189.

Rider, M.H., 1996. The Geological Interpretation of Wireline Logs. Whittles Publishing, Dunbeath.

Rowley, D. B., Xue, F., Tucker, R. D., Peng, Z. X., Baker, J., Davis, A., 1997. Ages of Ultrahigh-Pressure Metamorphism and Protolith Orthogneisses from the Eastern Dabieshan: U-Pb Zircon Geochronology. Earth and Planetary Science Letters, 151, 191–203

Sandiford, M., 2003. Neotectonics of southeastern Australia: linking the quaternary faulting record with seismicity and in situ stress. Geological Society of Australia Special Publication, 22, 101–113.

Serra, O., 2008. Well Logging Handbook. Paris, France, pp. 526-528.

Schlumberger, Ltd., 1994. FMI Fullbore Formation MicroImager: Houston, Texas (Schlumberger Educational Services), pp. 3-5.

Schmitt, D. R., Currie, C., Zhang, L., 2012. Crustal stress determination from boreholes and rock cores: Fundamental principles. Tectonophysics, 580, 1–26.

Schmitt, D. R., Haimson, B. C., 2016. Hydraulic Fracturing Stress Measurements in Deep Holes, Chapter 6, in Rock Mechanics and Engineering, Vol. 1, ed., X-T. Feng, CRC Press, 183-225

Sibson, R., Ghisetti, F., Ristau, J., 2011. Stress control of an evolving strike-slip fault system during the 2010–2011 Canterbury, New Zealand, earthquake sequence. Seismological Research Letters, 82 (6), 824–832.

Stein, R.S., 1999. The role of stress transfer in earthquake occurrence. Nature, 402 (6762), 605–609.

Stephen, M., 2009. Essentials of Geology. W.W. Norton & Co., New York.

Tingay, M., Reinecker, J., Müller, B., 2008. Borehole breakout and drilling-induced fracture analysis from image logs. World Stress Map Project Stress Analysis Guidelines. Available online at: www.world-stress-map.org.

Tingay, M., Hillis, R.R., Morley, C.K., King, R.C., Swarbrick, E., Damit, A.R., 2009. Present-day stress and neotectonics of Brunei: implications for petroleum exploration and production. AAPG Bulletin, 93, 75–100.

Vernik, L., Zoback, M.D., 1992. Estimation of the maximum horizontal principal stress magnitude from stress-induced wellbore breakouts in the Cajon Pass scientific research borehole. Journal of Geophysical Research, 97, 5109–5120.

Wan, T.F., Zhu, H., Zhao, L., Lin, J.P., Chen, J., Chen, J., 1996. Formation and evolution of the Tancheng-Lujiag fault zone: a review. Geoscience, 10 (2), 159–168 (in Chinese with English abstract).

Wang, X. M., Liou, J. G., Mao, H. K., 1989. Coesite-Bearing Eclogite from the Dabie Mountains, Central China. Geology, 17, 1085–1088.

Wu, H.Y., Ma, K.F., Zoback, M., Boness, N., Ito, H., Hung, J.H., Hickman, S., 2007. Stress orientations of Taiwan Chelungpu-fault Drilling Project (TCDO) hole-A as observed from geophysical logs. Geophysical Research Letter, 34, L01303.

Xu, S. T., Okay, A. I., Ji, S., 1992. Diamond from Dabie Shan Metamorphic Rocks and Its Implication for Tectonic Setting. Science, 256, 80–82

Xu, Z.Q., Wang, Q., Tang, Z.M., Chen, F.Y., 2009. Fabric kinematics of the ultrahigh pressure metamorphic rocks from the main borehole of the Chinese Continental Scientific Drilling Project: implications for continental subduction and exhumation. Tectonophysics, 475, 235–250

Zhang, J., Lang, J., Standifird, W., 2009. Stress, porosity, and failure dependent compressional and shear velocity ratio and its application to wellbore stability. Journal of Petroleum Science and Engineering, 69, 193–202.

Zhang, J., 2013. Borehole stability analysis accounting for anisotropies in drilling to weak bedding planes. International Journal of Rock Mechanics and Mining Sciences, 60, 160–170.

Zhang, R. Y., Hirajima, T., Banno, S., Cong, B., Liou, J.G., 1995. Petrology of Ultrahigh-Pressure Rocks from the Southern Su-Lu Region, Eastern China. Journal of

Metamorphic Geology, 13, 659–675

Zhang, Z. M., Shen, K., Xiao, Y. L., Hosfs, J., Liou, J.G., 2006. Mineral and fluid inclusions in zircon of UHP metamorphic rocks from the CCSD-main drill hole: a Record of metamorphism and fluid activity. Lithos, 92,378–398

Zhou, H., Ding, R., 1995. Study of the characteristics of crustal stress field in East China by inversion of nodal-plane data. Tectonophysics, 245(1-2), 53-59

Zhu, G., Wang, D.X., Liu, G.S., Niu, M.L., Song, C.Z., 2004. Evolution of the Tan-Lu fault zone and its responses to plate movement in west Pacific basin. Chinese Journal of Geology, 39 (1), 36-49 (in Chinese with English abstract).

Zoback, M.D., Moos, D., Mastin, L., Andersson, R.N., 1985. Well bore breakouts and in-situ stress. Journal of Geophysical Research, 90, 5523–5530.

Zoback, M.D., Barton, C.A, Brudy, M., Castillo, D.A., Finkbeiner, T., Grollimund, B.R., Moos, D.B., Peska, P., Ward, C.D., Wiprut, D.J., 2003. Determination of stress orientation and magnitude in deep wells. International Journal of Rock Mechanics and Mining Sciences, 40, 1049–1076.

Zoback, M. D., 2007. Reservoir geomechanics. Cambridge University Press, Cambridge, pp. 242-249.

Figure captions

Fig. 1. Preferential orientation of breakout and drilling induced tensile fracture (DITF) relative to the direction of the maximum horizontal principal stress in a vertical borehole (S_H: the maximum horizontal stress; S_h: the minimum horizontal stress) (modified after Rider, 1996; Hillis and Reynolds, 2000; Morin and Wilkens, 2005; Schmitt et al., 2012). (a) Horizontal cross-section of the borehole, (b) unrolled image of the borehole wall.

Fig. 2. Location of the CCSD borehole and its adjacent tectonic environment background. The inset shows the regional location with respect to nearby plate boundaries. (UHPM: Ultra-high pressure and metamorphic; YQWF: Yantai-Qingdao-Wulian Fault; JXF: Jiangshan-Xiangshui Fault; EU: Eurasian Plate; NA: North America Plate; PA: Pacific Plate; PH: Philippine Sea Plate; red arrows indicate the moving direction of the plate relative to the EU) (modified after Zhang et al. (2006) and Kimura et al. (2009))

Fig. 3. Some conventional logs and a simplified lithology profile of the CCSD borehole. (a) Gamma ray log (RG), (b) density log (DEN), (c) acoustic velocity log (V_p), (d) deep resistivity log (RD), (e) caliper log (CAL). (The lithology profile is modified from Liu et al. (2007) and Xu et al. (2009)). (The CAL log is very unstable and increased greatly in the 3000-3600 m interval due to the borehole enlargement operation).

Fig. 4. Identifying breakouts, drilling induced tensile fractures and nature fractures by Formation Micro-resistivity Image (FMI) and Ultra-Sonic (amplitude) Image (USI) logs from the CCSD borehole. (a) Borehole breakout (BO), (b) axial drilling induced tensile fracture (ADITF) and nature fracture (NF), (c) transverse drilling induced tensile fracture (TDITF). (Image logs are displayed unrolled clockwise and oriented to the geographic north.)

Fig. 5. An example of natural fracture features appearing on the Formation Micro-Resistivity Image (FMI) and Ultra-Sonic (amplitude) Image (USI) logs between 231 and 233 m of the CCSD borehole, together with relevant core image projected into azimuthal coordinates. (Image logs are displayed unrolled clockwise and oriented to the geographic north)

Fig. 6. An example of foliation and natural fracture (NF) features appearing on the Formation Micro-Resistivity Image (FMI) and Ultra-Sonic (amplitude) Image (USI) logs between 457 and 460 m of the CCSD borehole, together with relevant core image projected into azimuthal coordinates. Foliations appear more frequently on the resistivity image logs and display lots of fine and parallel stripes. Natural Fractures usually appear as dark (low-resistivity) quasi-sinusoidal stripes on both the resistivity and ultrasonic image logs and maybe parallel to the foliations.

Fig. 7. (a) The orientation of BO versus depth, (b) the orientations of ADITF and TDITF versus depth, (c) the direction of the S_H derived from the orientations of BO, ADITF and TDITF, (d) the dip azimuth of the CCSD borehole, (e) the deviation of the CCSD borehole, (f) the magnitudes of S_V, S_H and S_h versus depth (reused the magnitude data of S_H and S_h published by Cui et al. (2009) with permission granted by Elsevier). The rose diagram in panel (a), (b) and (c) showed the sample numbers and statistical features of the azimuth data set. (No useful image logs are recorded in the 3000-3600 m interval due to the borehole enlargement operation)

Fig. 8. Orientation of the present-day maximum horizontal principal stress in eastern China from the World Stress Map database (Heidbach et al., 2016) and from the CCSD borehole. (NF=normal faulting stress regime; SS=strike-slip faulting stress regime; TF=thrust faulting stress regime; U=undefined stress regime; Quality A=the direction of S_H is within ±15°; Quality B=the direction of S_H is within ±20°; Quality C=the direction of S_H is within ±25°).

Fig. 9. Fracture dip azimuth (θ_{in}) and frequency versus the depth of the borehole. (a) Dip azimuth for individual fractures, (b) fracture density in numbers of fractures per 10 meters

interval, (c) simplified lithology profile (modified from Liu et al. (2007) and Xu et al. (2009)). (no useful image logs are recorded in the 3000-3600 m interval due to the borehole enlargement operation)

Fig. 10. Rose diagrams of the dip azimuth of the natural fractures for different depth intervals (please note that image data are missing in the depth interval 3000-3600 m and cannot be analyzed). (a) 28-736 m; (b) 736-1113 m; (c) 1113-1596 m; (d) 1596-2038 m; (e) 2038-2280 m; (f) 2280-2920 m; (g) 3623-5000 m; (h) 28-5000 m.

Fig. 11. Rose diagrams of the dip azimuth of the foliations for different depth intervals (from Xu et al. (2009) with permission to reprint granted by Elsevier). (a) 0-736 m; (b) 736-1113 m; (c) 1113-1596 m; (d) 1596-2038 m; (e) 2038-2280 m; (f) 2280-2920 m; (g) 2920-3225 m; (h) 3225-5158 m.

Table captions

Table 1

Lithological unit (modified from Xu et al. (2009) with permission to reprint granted by Elsevier) and dip azimuth of fractures and foliations in each unit.

Figure

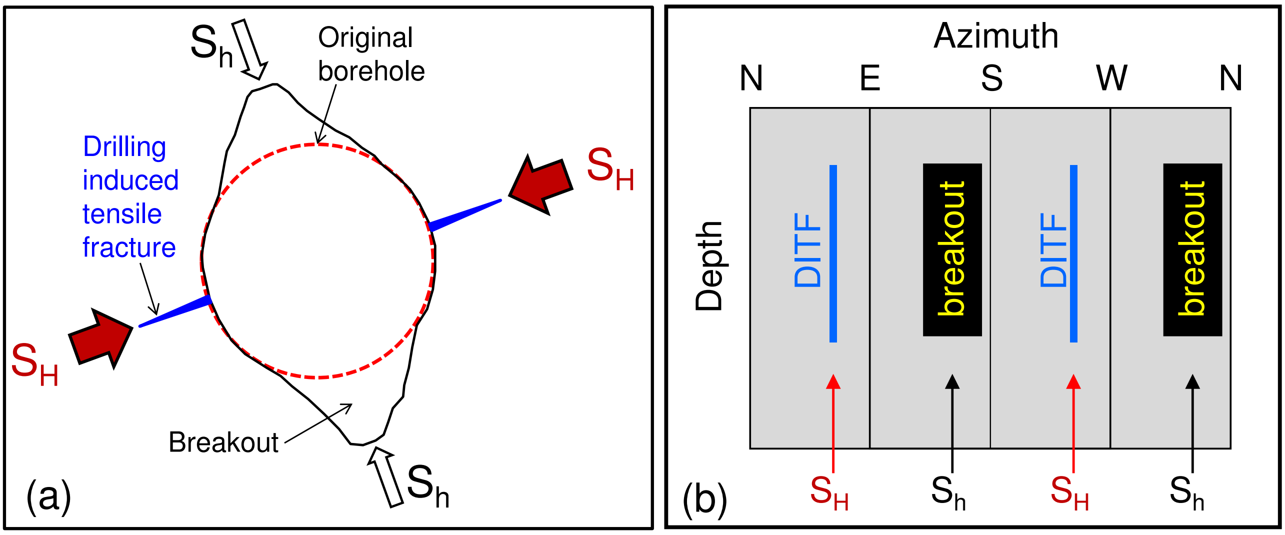

S_h
Original borehole
Drilling induced tensile fracture
S_H
S_H
Breakout
S_h
(a)
Azimuth
N
E
S
W
N
Depth
DITF
breakout
DITF
breakout
S_H
S_h
S_H
S_h
(b)

Fig. 1

Figure

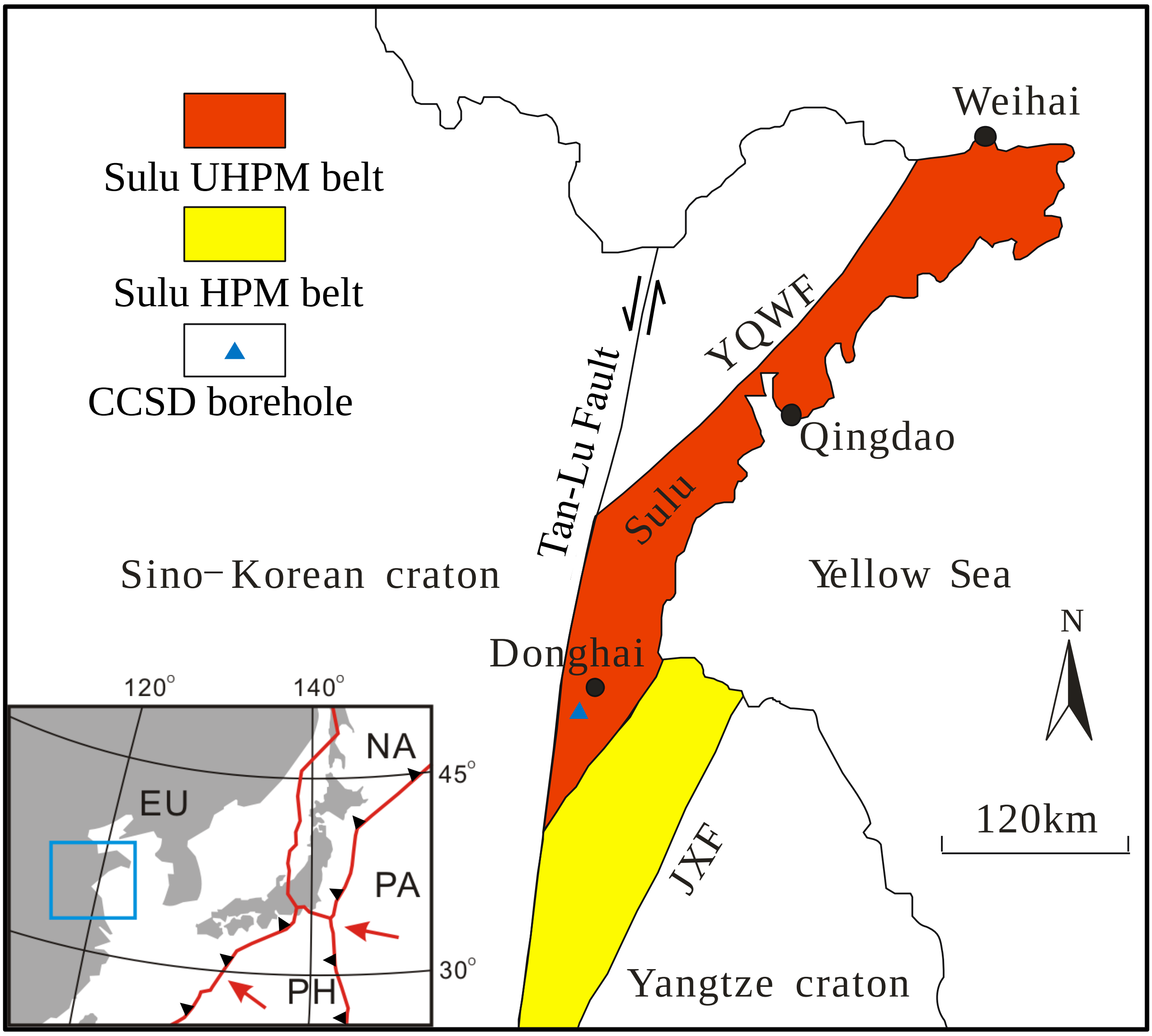

Sulu UHPM belt
Sulu HPM belt
CCSD borehole
Weihai
YQWF
Qingdao
Tan-Lu Fault
Sulu
Sino−Korean craton
Yellow Sea
Donghai
N
120km
JXF
Yangtze craton
120°
140°
NA
45°
EU
PA
30°
PH

Fig. 2

Figure

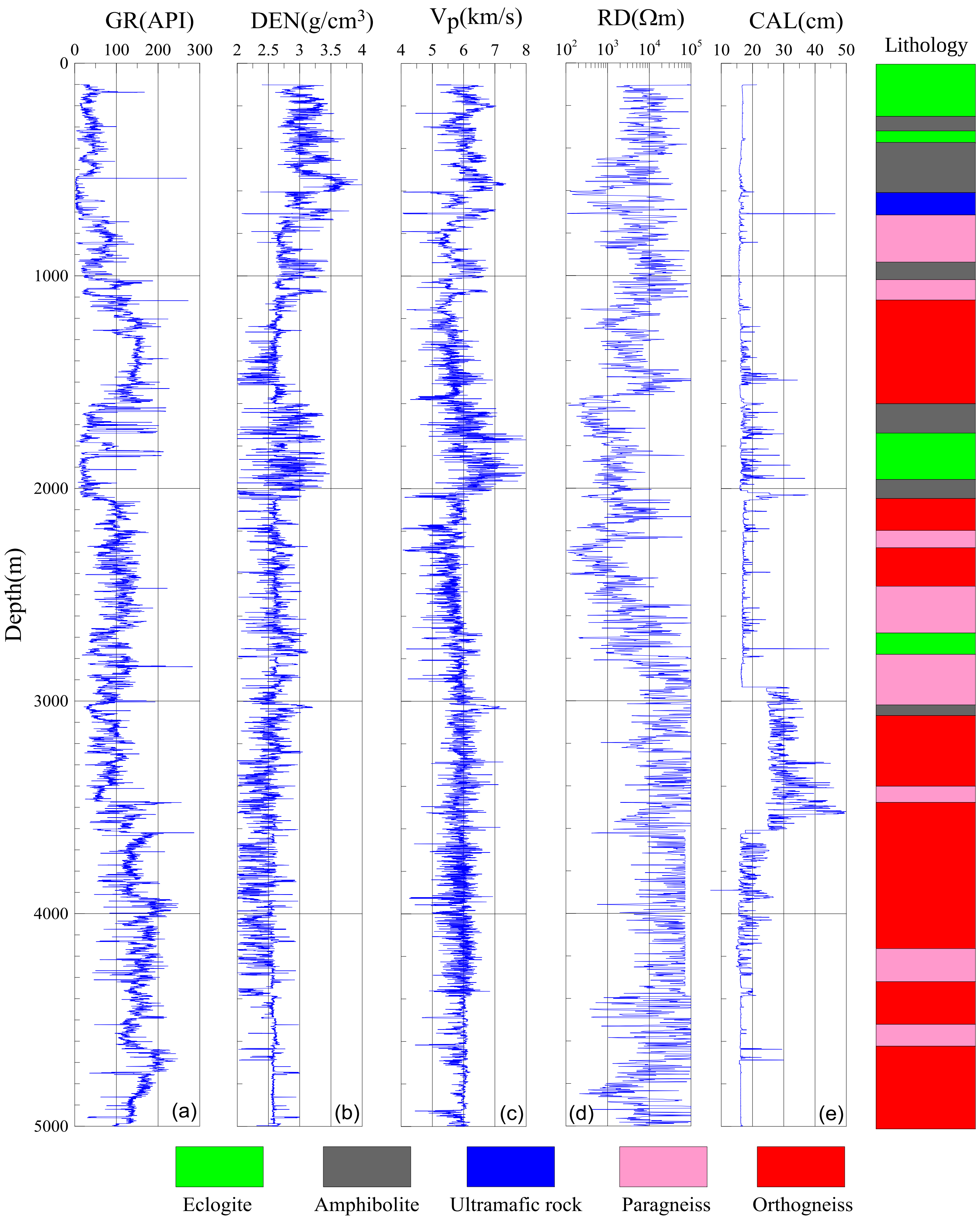

GR(API)
DEN(g/cm³)
Vp(km/s)
RD(Ωm)
CAL(cm)
Lithology
Depth(m)
0
100
200
300
2
2.5
3
3.5
4
4
5
6
7
8
10²
10³
10⁴
10⁵
10
20
30
40
50
1000
2000
3000
4000
5000
(a)
(b)
(c)
(d)
(e)
Eclogite
Amphibolite
Ultramafic rock
Paragneiss
Orthogneiss

Fig. 3

Figure

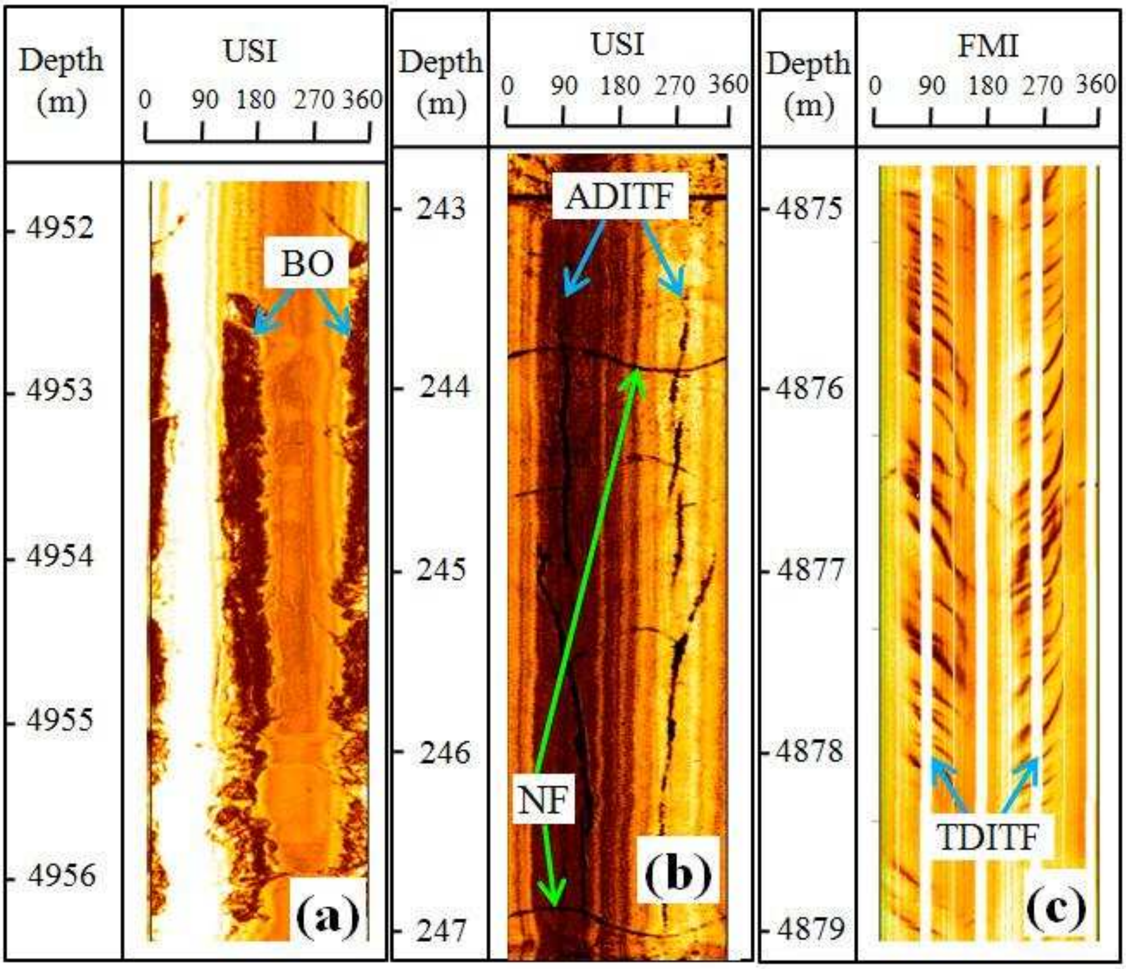
Depth (m)
USI
0 90 180 270 360
4952
4953
4954
4955
4956
BO
(a)
Depth (m)
USI
0 90 180 270 360
243
244
245
246
247
ADITF
NF
(b)
Depth (m)
FMI
0 90 180 270 360
4875
4876
4877
4878
4879
TDITF
(c)

Fig. 4

Figure

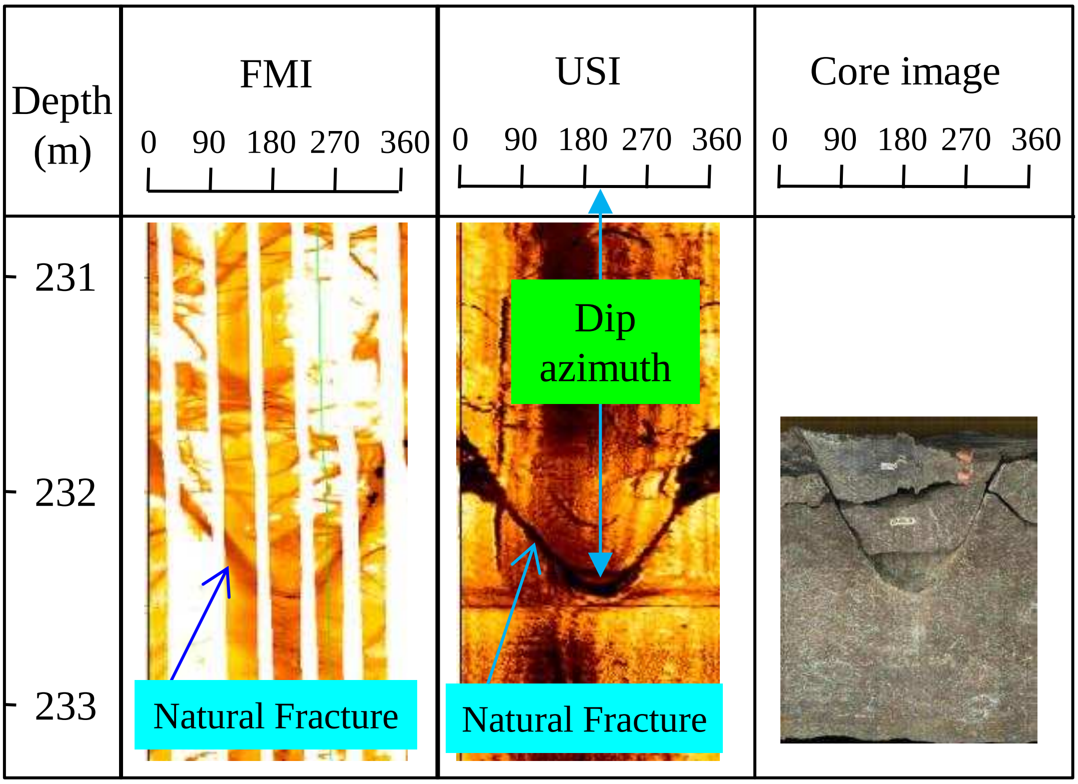
Depth (m)
FMI
USI
Core image
0 90 180 270 360
0 90 180 270 360
0 90 180 270 360
231
232
233
Dip azimuth
Natural Fracture
Natural Fracture

Fig. 5

Figure

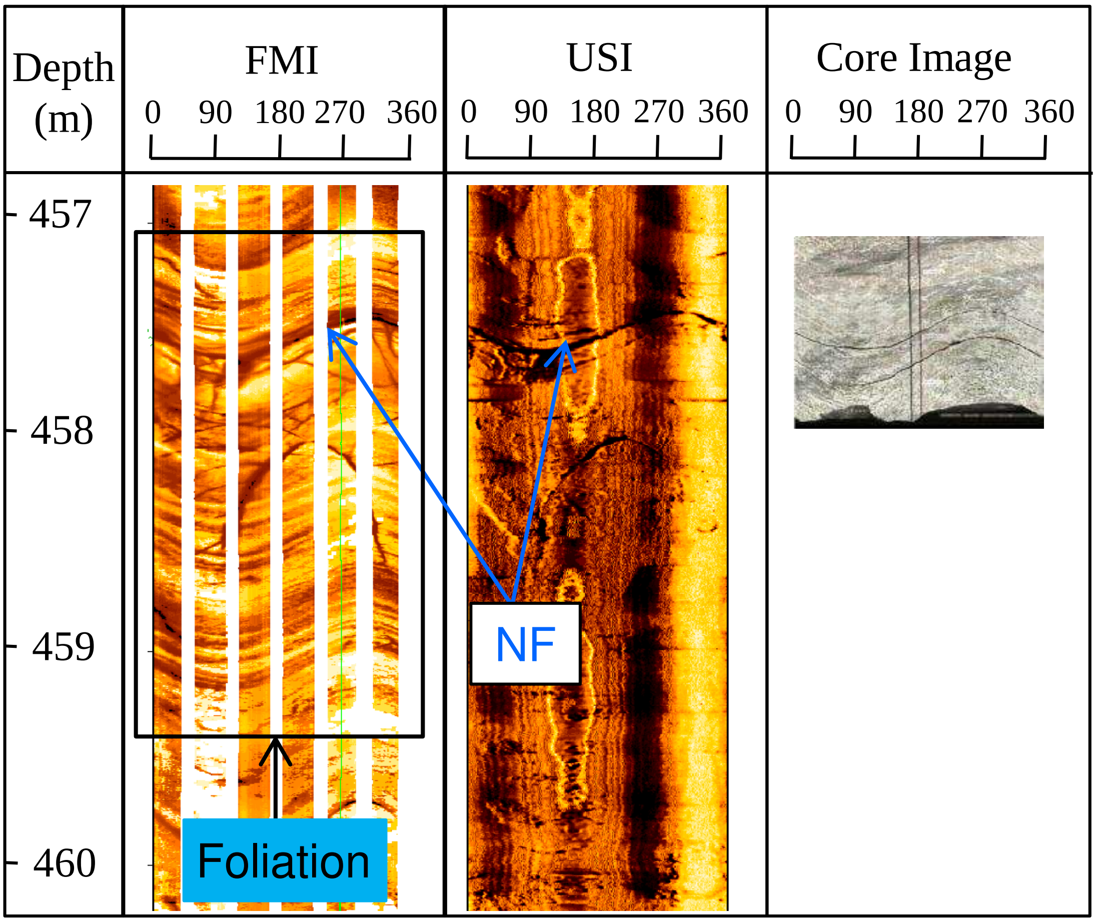

Depth (m)
FMI
USI
Core Image
0 90 180 270 360
0 90 180 270 360
0 90 180 270 360
457
458
459
460
NF
Foliation

Fig. 6

Figure

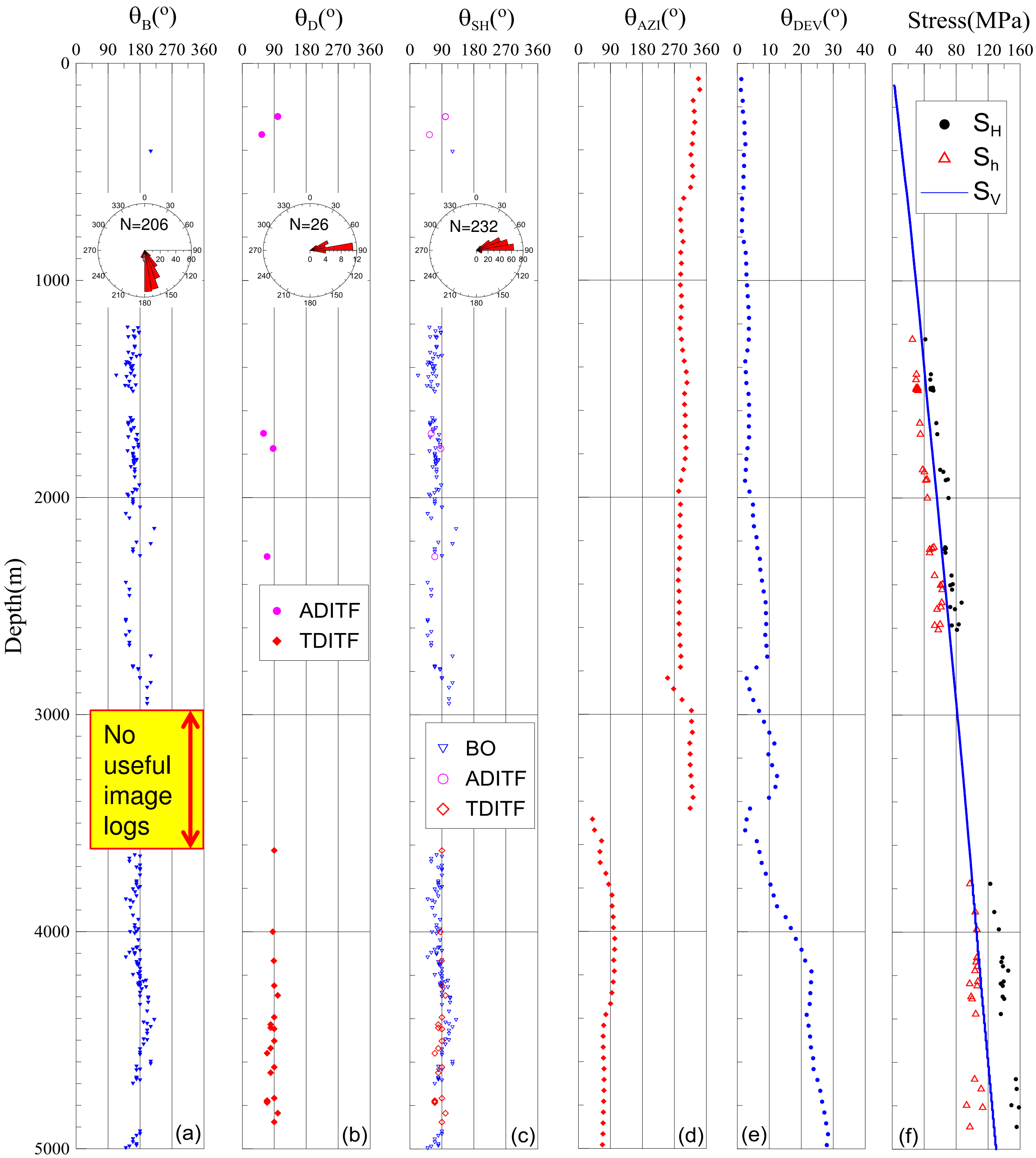

θB(o)
θD(o)
θSH(o)
θAZI(o)
θDEV(o)
Stress(MPa)
Depth(m)
N=206
N=26
N=232
No useful image logs
ADITF
TDITF
BO
SH
Sh
SV
(a)
(b)
(c)
(d)
(e)
(f)

Fig. 7

Figure

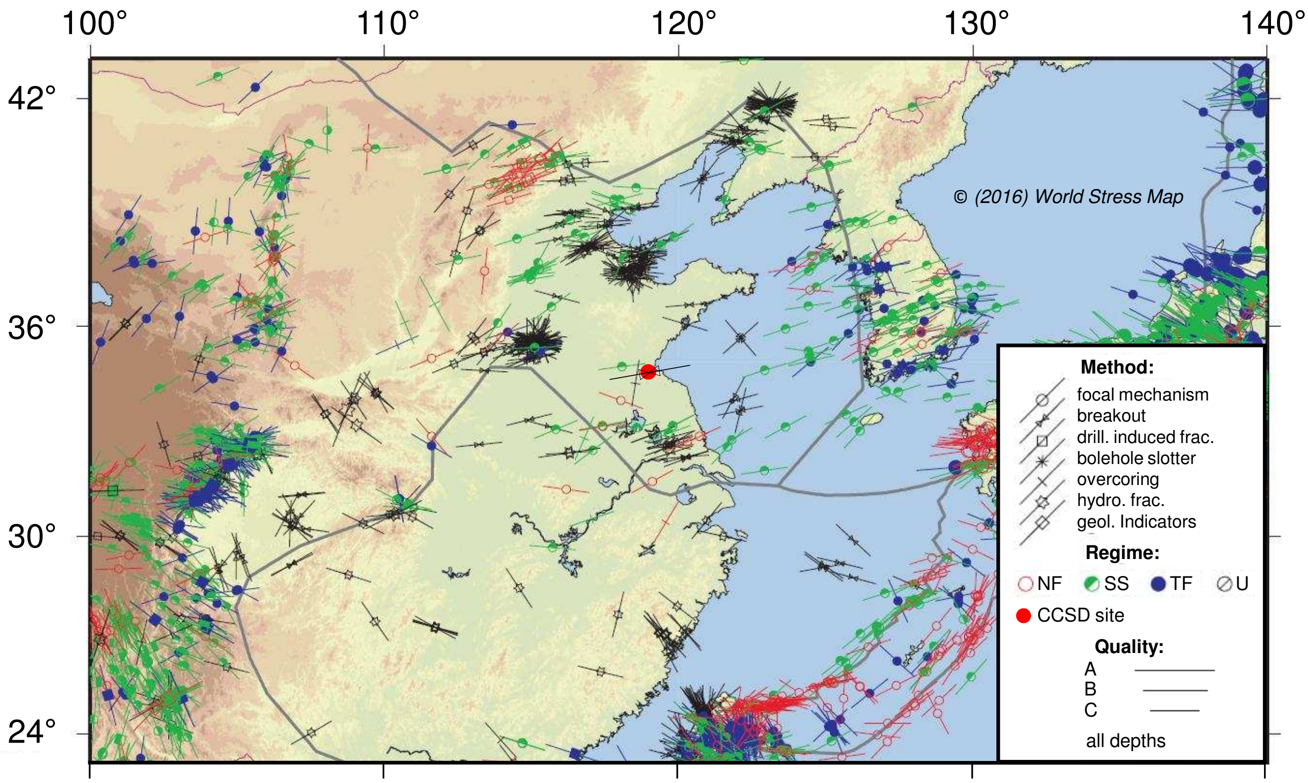
100°
110°
120°
130°
140°
42°
36°
30°
24°
© (2016) World Stress Map
Method:
focal mechanism
breakout
drill. induced frac.
bolehole slotter
overcoring
hydro. frac.
geol. Indicators
Regime:
NF
SS
TF
U
CCSD site
Quality:
A
B
C
all depths

Fig. 8

Figure

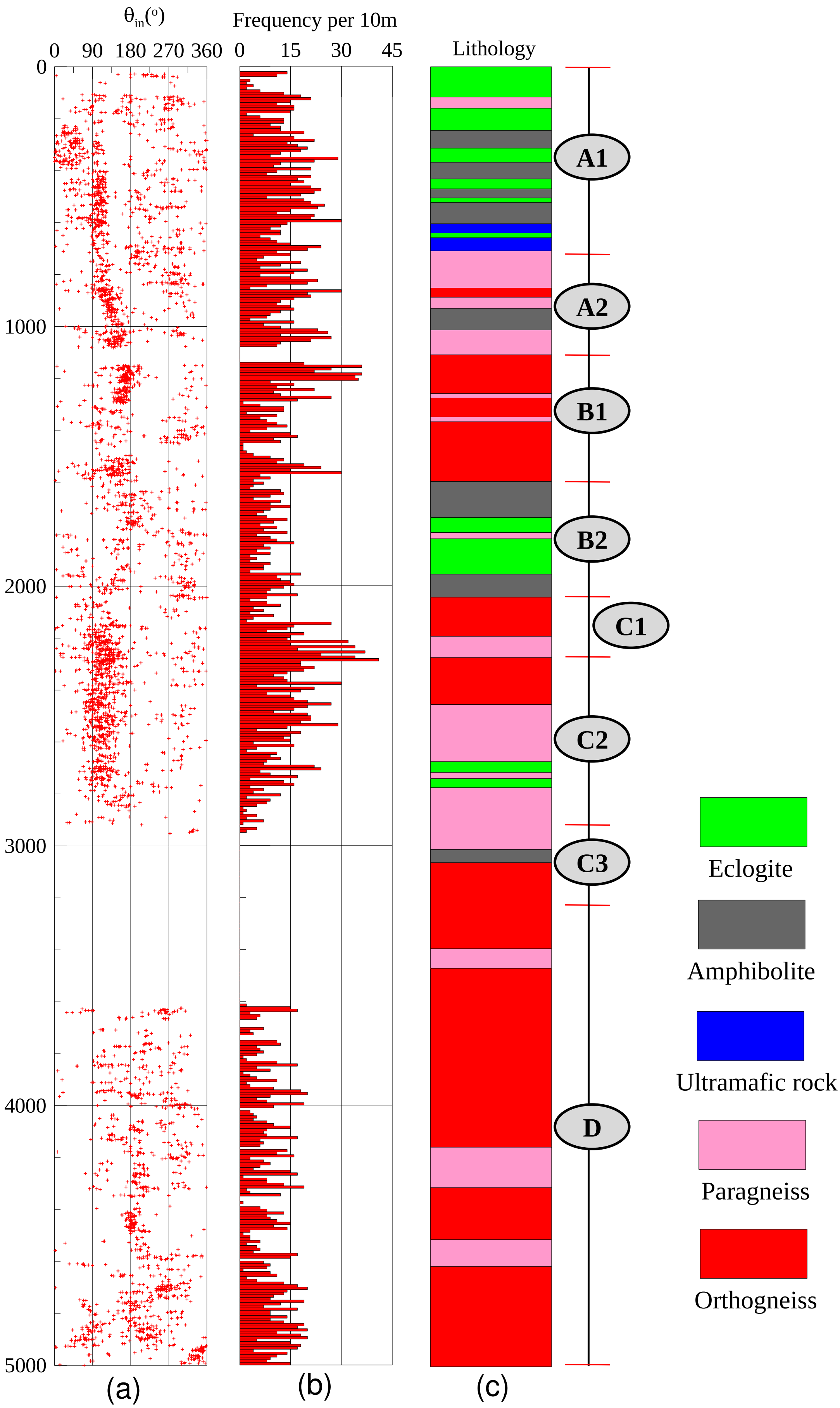

θ_{in}(°)
0 90 180 270 360
Frequency per 10m
0 15 30 45
Lithology
0
1000
2000
3000
4000
5000
A1
A2
B1
B2
C1
C2
C3
D
Eclogite
Amphibolite
Ultramafic rock
Paragneiss
Orthogneiss
(a)
(b)
(c)

Fig. 9

Figure

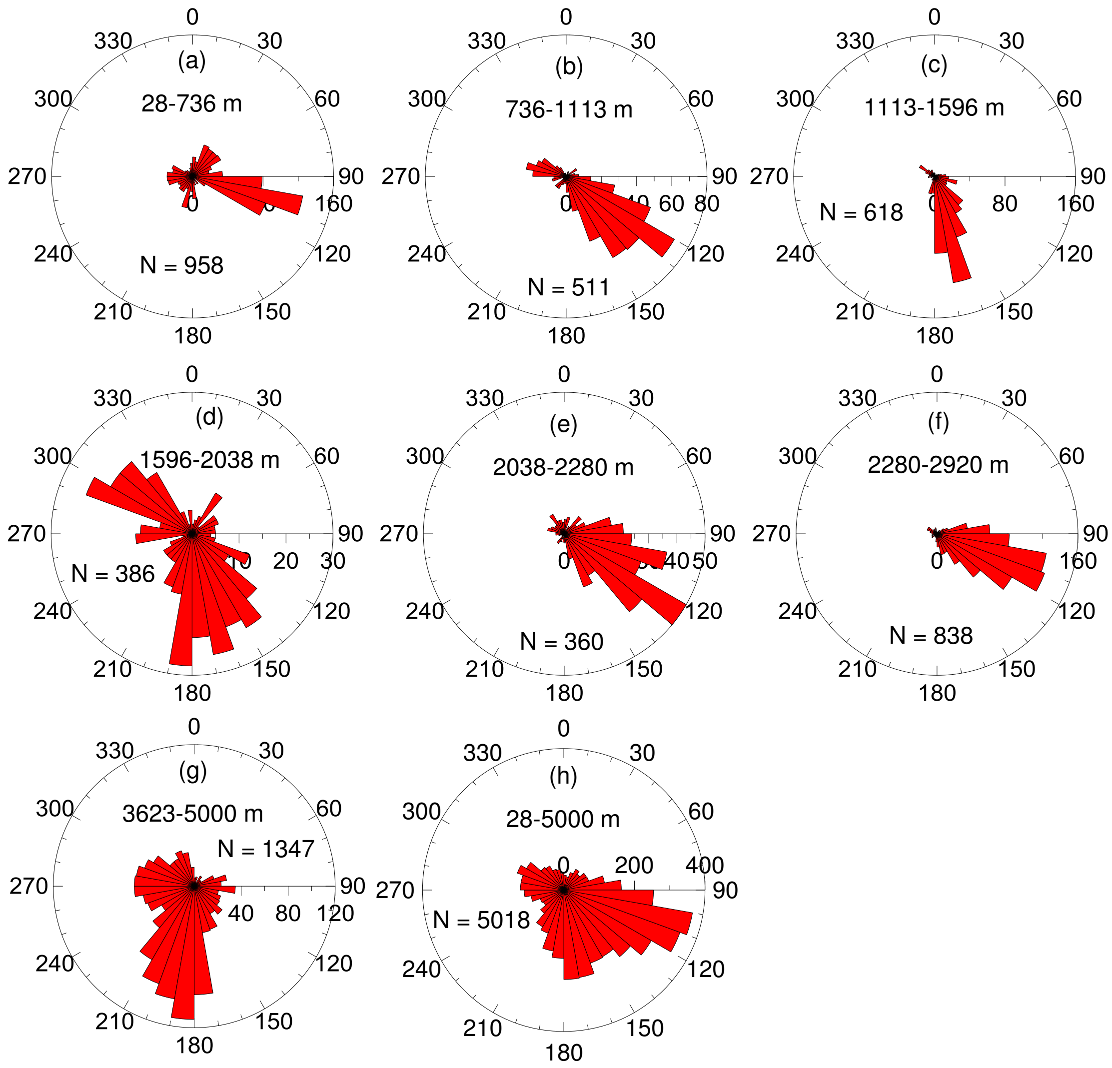

Fig. 10

Figure

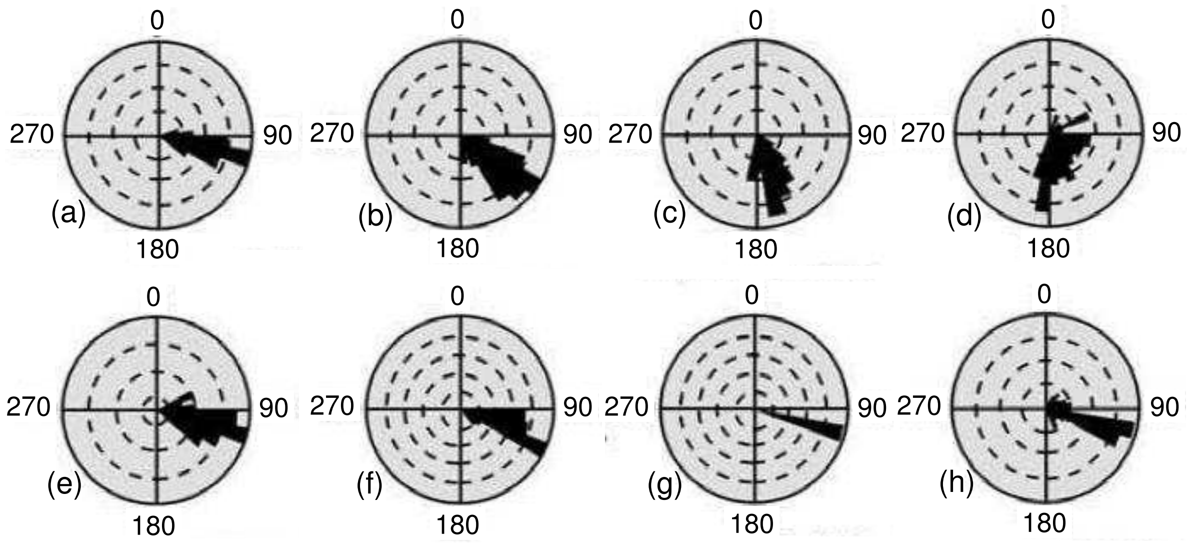

Fig. 11

Table 1

Unit	Depth (m)	Lithology	Fig. 10	Dip direction of fractures	Fig. 11	Dip direction of foliations
A1	0-736	eclogite	(a)	110±10°	(a)	110±10°
A2	736-1113	paragneiss	(b)	130±20°	(b)	135±10°
B1	1113-1596	orthogneiss	(c)	165±10°	(c)	160±10°
B2	1596-2038	eclogite	(d)	165±20°	(d)	180±15°
C1	2038-2280	orthogneiss	(e)	120±20°	(e)	110±10°
C2	2280-2920	paragneiss	(f)	110±15°	(f)	110±5°
C3	2920-3225	paragneiss and orthogneiss	-	-	(g)	105±5°
D	3225-5158	orthogneiss and paragneiss	(g)	200±20°	(h)	110±10°

Graphical Abstract (for review)